

PAPER • OPEN ACCESS

Three-dimensional Fabry–Pérot cavities sculpted on fiber tips using a multiphoton polymerization process


To cite this article: Jonathan W Smith *et al* 2020 *J. Micromech. Microeng.* **30** 125007

View the [article online](#) for updates and enhancements.

You may also like

- [A high-efficiency C-band coaxial transit time oscillator with a dual-cavity extractor under low-magnetic fields](#)
Danni Zhu, Yancheng Cui, Jin Meng et al.
- [Optical self-injection mode-locking of semiconductor optical amplifier fiber ring with electro-absorption modulation—fundamentals and applications](#)
Yu-Chieh Chi and Gong-Ru Lin
- [Controllable four-wave mixing response in a dual-cavity hybrid optomechanical system](#)
Lei Shang, , Bin Chen et al.

Three-dimensional Fabry–Pérot cavities sculpted on fiber tips using a multiphoton polymerization process

Jonathan W Smith¹, Jeremiah C Williams¹, Joseph S Suelzer², Nicholas G Usechak² and Hengky Chandralim¹ 

¹ Department of Electrical and Computer Engineering, the US Air Force Institute of Technology, Wright–Patterson Air Force Base, Ohio 45433, United States of America

² Air Force Research Laboratory, Wright–Patterson Air Force Base, Ohio 45433, United States of America

E-mail: Hengky.Chandralim@afit.edu

Received 19 June 2020, revised 27 August 2020

Accepted for publication 14 October 2020

Published 23 October 2020



CrossMark

Abstract

This paper presents 3D Fabry–Pérot (FP) cavities fabricated directly onto cleaved ends of low-loss optical fibers by a two-photon polymerization (2PP) process. This fabrication technique is quick, simple, and inexpensive compared to planar microfabrication processes, which enables rapid prototyping and the ability to adapt to new requirements. These devices also utilize true 3D design freedom, facilitating the realization of microscale optical elements with challenging geometries. Three different device types were fabricated and evaluated: an unreleased single-cavity device, a released dual-cavity device, and a released hemispherical mirror dual-cavity device. Each iteration improved the quality of the FP cavity's reflection spectrum. The unreleased device demonstrated an extinction ratio around 1.90, the released device achieved 61, and the hemispherical device achieved 253, providing a strong signal to observe changes in the free spectral range of the device's reflection response. The reflectance of the photopolymer was also estimated to be between 0.2 and 0.3 over the spectrum of interest. The dual-cavity devices include both an open cavity, which can interact with an interstitial medium, and a second solid cavity, which provides a static reference reflection. The hemispherical dual-cavity device further improves the quality of the reflection signal with a more consistent resonance, and reduced sensitivity to misalignment. These advanced features, which are very challenging to realize with traditional planar microfabrication techniques, are fabricated in a single patterning step. The usability of these FP cavities as thermal radiation sensors with excellent linear response and sensitivity over a broad range of temperature is reported. The 3D structuring capability the 2PP process has enabled the creation of a suspended FP heat sensor that exhibited linear response over the temperature range of 20 °C –120 °C; temperature sensitivity of $\sim 50 \text{ pm } ^\circ\text{C}^{-1}$ at around 1550 nm wavelength; and sensitivity improvement of better than 9x of the solidly-mounted sensors.

Keywords: Fabry–Pérot, multiphoton polymerization, 3D microfabrication, optical sensors, fiber tip sensors

(Some figures may appear in colour only in the online journal)



1. Introduction

The Fabry–Perot (FP) cavity is an important optical component with many applications. A basic FP cavity consists of two parallel reflective surfaces separated by a chosen distance and encapsulating air, vacuum, or another media with refractive index (RI) n . Multiple beam interference between the two surfaces causes transmission through the cavity to peak at specific wavelengths of maximum coherent interference, while others are reflected. At the micron scale, this enables the FP cavity to propagate a small number of optical modes compared to other optical cavities such as ring resonators, photonic crystals, and distributed feedback gratings [1]. The FP cavity can also achieve large quality factors, with values as high as 10^5 reported [2]. It is easily accessible to the environment and, unlike devices such as the ring resonator, the FP cavity does not require the substance inside the cavity to have a different RI than the substance outside the cavity [3]. While often beneficial, the open nature of the FP cavity means it lacks lateral confinement, and loses some resonant light off the edges of the mirrors. Flat FP cavities are highly sensitive to misalignment, and any misalignment, even one of several degrees, between the mirrors will significantly lower a cavity's quality factor [1]. One popular way to overcome this sensitivity is by using one or more curved mirrors [3–5], although this often increases the complexity of fabrication. This work introduces an innovative fabrication process that greatly simplifies the realization of complex geometries on virtually any substrate.

Many advantages of the FP cavity have made it a key component to a myriad of applications. When used to form a laser cavity, a variety of exotic gain media have recently been explored including biological tissues [6], silicon nanowires [7], and optical fluids [1, 3]. Miniaturized tunable lasers [8, 9] and tunable optical filters [10] have also been realized by integrating an FP cavity with microelectromechanical systems. The accessibility of the cavity has also made it a powerful tool for spectroscopy. It has been used in on-chip microfluidics [11], human breath analysis [12], interrogation of living cells [13], and compact imaging spectrometers [14]. The FP cavity is also set to play a key role in the emerging field of quantum computing, with cavity quantum electrodynamics at the forefront of many advances. It has been demonstrated in a photon emission source [4, 15], in strong coupling to a trapped atom [16], and in frequency splitting of polarization Eigen modes [17, 18].

The difference between two resonant wavelengths in a FP cavity, the cavity's free spectral range (FSR), is determined by the distance between the mirrors and the refractive index of the medium inside the cavity. Sensors can detect phenomena that affect these factors, and have found many applications to include sensing gravitational waves [19], acceleration [20], pressure and refractive indices of liquids [21], temperature [22], force [23], and even gas composition [24].

Optical fibers present a powerful platform to both form and interrogate FP cavities due to their small form factor, low-loss, and well-behaved transverse optical mode structure. Promising applications for fiber integrated FP cavities include optofluidic in-fiber lasers [25, 26] and miniaturized high sensitivity sensors [21–24]. Poor lateral confinement and misalignment

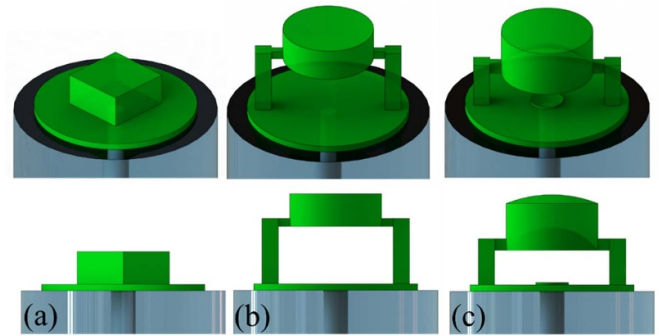


Figure 1. Schematic views of the FP cavity devices. (a) The single-cavity, (b) the released dual-cavity, and (c) the released hemispherical dual-cavity devices on cleaved ends of optical fibers.

sensitivity continue to plague fiber based FP cavity devices, and represent significant design challenges. The fiber itself is also an exotic substrate due to its geometry, which renders it incompatible with many planar microfabrication processes. A variety of techniques have been explored to overcome these challenges and create FP cavities on optical fibers. One device was fabricated by splicing a segment of hollow-core optical fiber (HOF) to a single-mode fiber (SMF), and capping the HOF with a segment of photonic crystal fiber (PCF) [24]. While this design can interrogate gasses, liquids would have difficulty reaching the cavity through the small openings in the PCF. Splicing various types of optical fibers also requires precise alignment and may be difficult to repeat reliably. Another successful on-fiber FP resonator was made by ion milling a cavity into a tapered SMF probe [22]. While the environment is easily accessed by this cavity, the fabrication process is complex and laborious, involving CO₂ laser pulling and metal deposition before the ion milling. Another group used the photo-active polymer SU-8 to construct a suspended polymer cavity on a fiber tip [21]. The resulting device can interrogate liquid or gas, and the fabrication process enables 2D freedom with a digital mirror. But this process is also relatively complicated, requiring a spray coat, bake, and UV exposure for each individual layer. This also limits the 3D structures that can be realistically built.

The devices presented in this work were fabricated using a simple process that requires only mounting the fiber into a two-photon polymerization (2PP) system from Nanoscribe GmbH and chemical developing [27]. This technique enabled us to realize 3D free-form geometries—a feat which cannot be accomplished using other methods on this spatial scale. This enables the use of nonplanar components to improve device performance, such as in our use of curved mirrors to create a hemispherical FP cavity to significantly reduce misalignment susceptibility. Our method can create these 3D components with submicron precision. The three on-fiber FP cavity designs that were fabricated and tested are depicted in figure 1. The hemispherical device achieved the greatest extinction ratio of the three designs tested, and highlights the power of the design freedom afforded by this process. The unreleased device demonstrated an extinction ratio around 1.90, the released device achieved 61, and the hemispherical

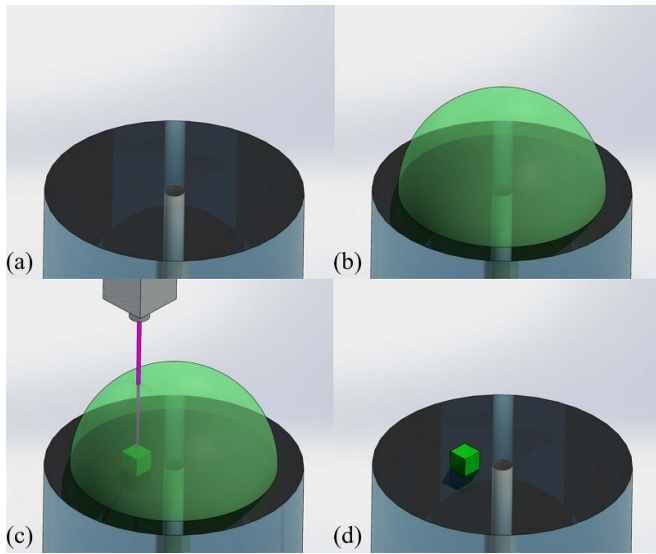


Figure 2. An example of the two-photon polymerization microfabrication process flow (devices fabricated in this work were centered on the fiber core). (a) The fiber tip was properly cleaned, cleaved, and mounted on a laser machining station. (b) Photosensitive IP-DIP resin (marketed by Nanoscribe GmbH) was deposited on the fiber tip. (c) A femtosecond laser was then focused in the resin to polymerize portions of resin layer by layer. (d) A chemical developer was used to remove non-polymerized resin, releasing the solidified structure.

device achieved 253, providing a strong signal to observe changes in the FSR of the device. We were also able to extract the reflectance of the photopolymer by fitting an Airy distribution to the reflection spectrum. This yielded a reflectance between 0.2 and 0.3 for the polymerized resin. The dual-cavity devices allow for interrogation of an interstitial medium in the first, open cavity while simultaneously referencing the static reflection spectrum of the second, solid-polymer cavity. These advanced features, which are very difficult or impossible to achieve with traditional planar microfabrication techniques, were fabricated in a single patterning step. The speed and simplicity of fabrication enables rapid prototyping and iterative design processes to realize complicated devices and advanced features.

2. Fabrication process

The maskless 2PP fabrication process used to fabricate all devices demonstrated in this work is outlined in figure 2. First the optical fiber was stripped, cleaned, and cleaved to create a flat platform with access to the core of the fiber, as illustrated in figure 2(a). The optical fiber used in this work was F-SM1500-9/125-P fiber from Newport Corporation. The cleaved fiber was secured into a Newport FPH-S fiber chuck and mounted into a custom jig that aligned the cleaved fiber face orthogonally to the laser aperture of the Nanoscribe GmbH system. The uncured, liquid photoactive polymer resin (Nanoscribe's IP-DIP) was deposited onto the cleaved fiber face, as shown in figure 2(b). The resin can be deposited in

any thickness or shape that encloses the desired build volume. Thus, several traditional photoresist deposition steps, such as spin-coating and pre-baking, were eliminated.

Once mounted, the resin was selectively exposed to ultrashort laser pulses with a wavelength of 780 nm, a repetition rate of 80 MHz, and a pulse duration of 120 fs by the Nanoscribe GmbH laser writing system. The resin only solidified when subjected to the nonlinear optical process of 2PP. Simultaneous absorption of two photons was necessary to polymerize the resin, which only occurred in a small portion of the focused laser beam [28]. The volume of the beam initiating 2PP can be scaled to offer a balance of resolution and speed. The minimum volume for this system was 150 nm wide by 150 nm long by 200 nm tall. This focal point was scanned through the resin according to a computer-aided design file to solidify the desired structure. This is pictured in figure 2(c). This system has a maximum scan speed of 2 mm s^{-1} , but small features and optical quality curvatures require significantly slower scan speeds. The FP cavity devices in this work were fully polymerized in less than 15 min. The x-y aspects of each layer were controlled by a galvanometer, while the z direction was controlled with a piezoelectric actuator.

Once the desired volume had been polymerized, the fiber tip was submerged in propylene glycol methyl ether acetate (PGMEA) for 20 min. This common solvent removed the unexposed resin, releasing the polymerized structure. Finally, the fiber tip was submerged in isopropanol for another 20 min to clean off the PGMEA. The result was the desired 3D structure of polymerized resin as illustrated in figure 2(d).

While significantly faster than other fabrication methods, the stepwise nature of the laser scanning process introduced striations into the surface finish of the devices. Planar FP cavities require a flat reflective surface, and hemispherical FP cavities require a smooth spherical mirror, and it was not known if the devices created here had an optical-quality surface finish. Also of concern, features with a height equal to one half or one quarter of the wavelength of interest could introduce destructive interference and create an antireflective surface. To analyze the surface finish, we fabricated a sample structure onto an indium-tin-oxide coated glass slide to mount into an atomic force microscope (AFM).

The resultant AFM scans are included in figure 3. The expected striations from the scanning process were present at regular intervals. The surface finish, including these features, was found to have a roughness of approximately 60 nm, with the peak to peak difference averaging 120 nm. This work focused on using wavelengths in the 1460–1640 nm range to probe the FP structures fabricated on the fiber ends. Therefore, the fabrication variations in surface roughness are significantly smaller than the wavelengths of interest, and far less than one half or one quarter wavelength interval which would lead to their own interference effects. In fact, the structures fabricated by this process were confirmed to have a roughness below $\lambda/10$ which is consistent with an optical quality surface finish in the wavelengths of interest.

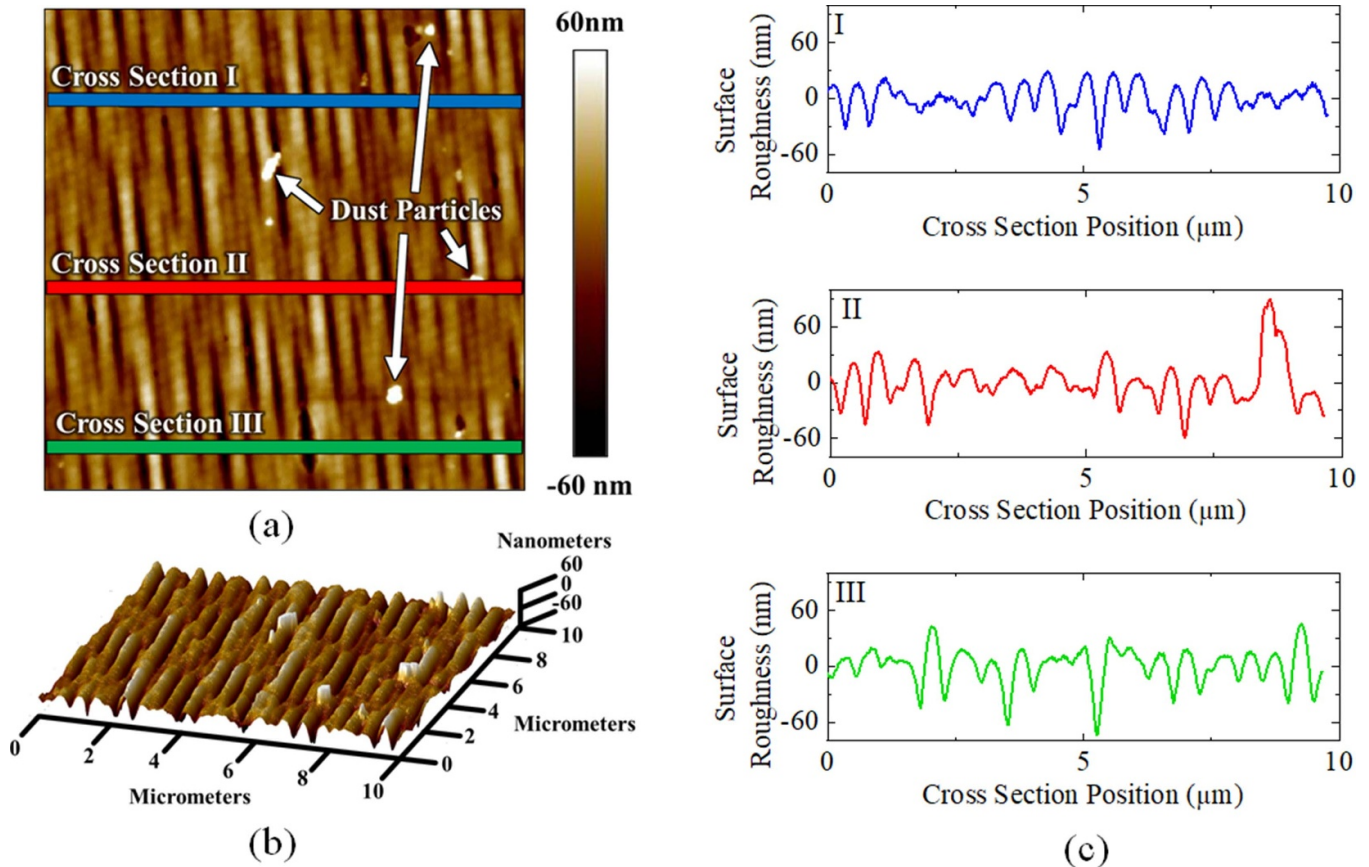


Figure 3. Surface analysis of an optical flat fabricated with two-photon polymerization by ultrashort laser pulses. (a) AFM image of the surface interrogated. (b) A 3D rendering of the AFM scan showing surface topography. (c) Three cross sections throughout the surface to quantify roughness.

3. Device characterization

3.1. Measurement setup

The FP cavities were characterized according to the measurement setup pictured in figure 4. All experiments were performed in a temperature-controlled laboratory that has a temperature of 20 °C with fluctuations of less than 2 °C. A tunable laser source (Agilent 81600B) was connected to the first port of an optical circulator. This was swept from 1463 nm to 1634 nm during each measurement. The SMF with an FP cavity device was fusion spliced to another SMF terminating in an FC/APC connector using a Fujikura FSM-100P ARC Master fiber splicer. This was connected to the second port of the optical circulator. The third port of the optical circulator was connected to a Newport universal fiber optic detector. This photodetector interfaced with a Newport 1830-C optical power meter, whose output was visualized and stored using a Keysight D509254A digital storage oscilloscope.

The variable laser source was then swept from 1463 nm to 1634 nm and the reflection from the FP cavity device was isolated by the optical circulator. The photodetector and power meter transduced the optical power into a voltage which was recorded by the oscilloscope. Optical resonances within the FP cavity caused a peak in transmission through the cavity which was observed as a dip in reflection intensity. This

technique allowed the devices to be used remotely, with the bulky input and measurement components geographically separated from the device. In this work the optical circulator and input fiber were polarization maintaining, while the device fiber (and the fabricated FP cavities) were not. Polarization maintaining fibers can be used to insure operation using a single polarization which could prove important for very long standoff detectors where polarization mode dispersion could reduce fringe visibility.

The reflection spectrum of each device was measured in volts read by the oscilloscope at a given wavelength. The extinction ratio reported for each device was calculated using the ratio between the mean of the four lowest reflection dips and the mean of the four highest reflection peaks. The mean of the four highest peaks is referred to as the high reflection intensity, and the mean of the four lowest dips is referred to as the low reflection intensity. Assuming incident light normal to each cavity, the theoretical FSR of a FP cavity is calculated according to $\Delta\lambda_{\text{FSR}} = \lambda_0^2/2nl$, where λ_0 is the central wavelength of the transmission peak (and reflection dip), n is the RI of the cavity medium, and l is the length of the cavity. For our devices, we considered a hypothetical transmission peak at 1550 nm, an IP-DIP refractive index of 1.504, and a refractive index of 1 in air. The RI was calculated by interpolating data provided by Nanoscribe, and 1550 nm is a common

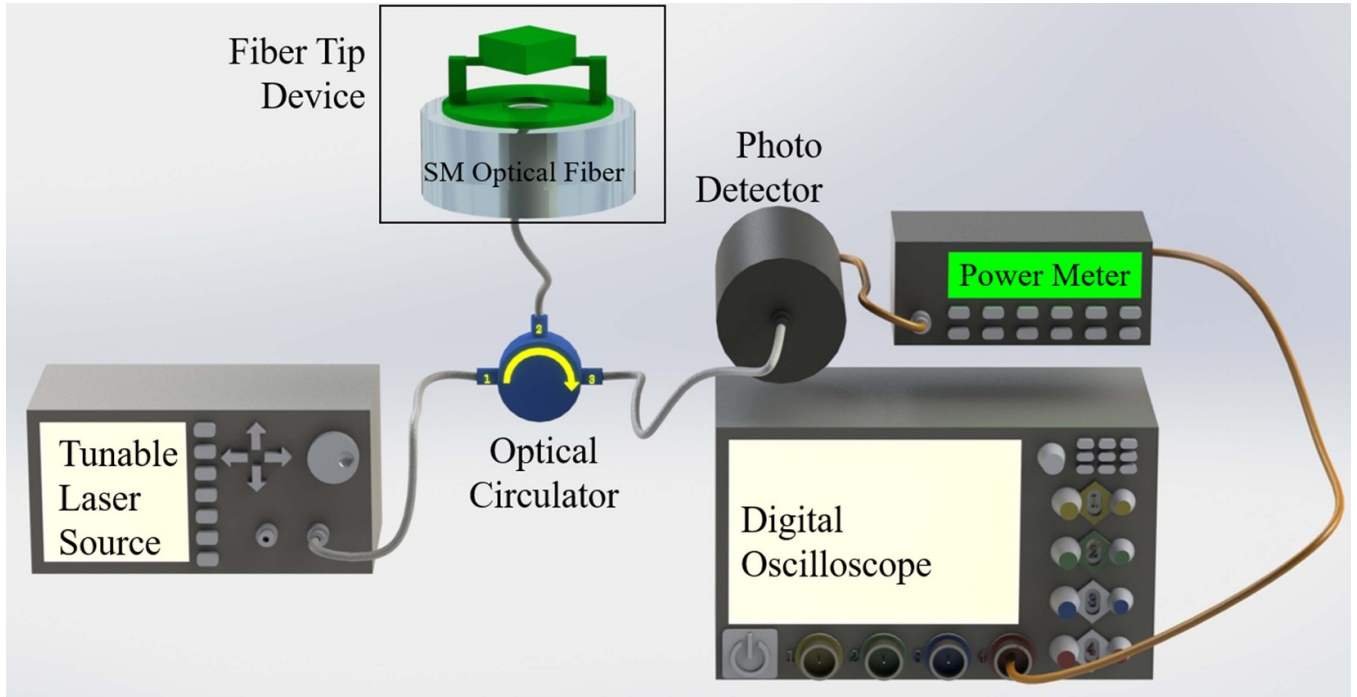


Figure 4. Diagram of the experimental setup used to characterize the reflection spectrum of each device in air at room temperature.

telecom wavelength in the middle of our laser's bandwidth. All calculations assume room temperature.

The transmission through a FP resonator can be modelled by the Airy distribution, which calculates the internal resonance enhancement factor for light of a given wavelength based on the physical properties of the cavity [29]. The generic Airy distribution for two mirrors of equal reflectance is calculated with, $A = \left[(1 - R)^2 + 4R\sin^2(\phi) \right]^{-1}$, where R is the reflectance of the mirrors, and 2ϕ is the single-pass phase shift between the mirrors [29]. This is calculated with, $2\phi = 2\pi\nu/\Delta\nu_{\text{FSR}} \approx 2\pi\lambda/\Delta\lambda_{\text{FSR}}$. The intensity of light reflected back from the cavity, as was measured in this work, is inversely proportional to the transmission intensity.

We extracted the reflectance of the mirrors in our devices by fitting an Airy distribution to the measured reflection spectrum. To create a comparable waveform, we selected the FSR and first λ_0 from our measurements, and centered the phase shift at the initial resonant wavelength by subtracting it from λ to determine the single-pass phase shift in relation to the resonant wavelength, $2\phi' = 2\pi(\lambda - \lambda_0)/\Delta\lambda_{\text{FSR}}$. The distribution was also normalized and scaled to the maximum and minimum voltage readings for each device. For the dual-cavity devices, the FSR and initial resonant wavelengths of each cavity were used to calculate two Airy distributions, which were added together, then normalized and scaled to the magnitude of the measured reflection. This showed the ideal response of each device given the measured FSR, resonant wavelength, and magnitude. With this waveform, different values of R were chosen until the magnitude and shape closely resembled the measured response. The value that provided the best match was taken as the reflectance.

3.2. Measurement results

A scanning electron microscope (SEM) image of the fabricated single-cavity device is presented in figure 5(a), while the measured reflection intensity is presented in figure 5(b). The cavity was formed by a 17.58 μm long, 40 μm by 40 μm rectangle, resulting in a theoretical FSR of 45.43 nm. The measured average $\Delta\lambda_{\text{FSR}}$ was 42.09 nm, showing a variation of only 3.34 nm. The device's high reflection intensity was 19.29 μW corresponding to a voltage of 132.58 mV. The low reflection intensity was 10.17 μW with a voltage of 69.89 mV, yielding an extinction ratio of 1.90. Fitting the Airy distribution to these results gave a reflectance of 0.01. This low value was caused by the thicker fiber-polymer interface, as the released devices show significantly higher reflectance. The corresponding Airy distribution is included in figure 5(c).

The single-cavity device confirmed that the 2PP method successfully produced optical elements for planar FP resonators. The released dual-cavity device represents a significant improvement in functionality over the single-cavity device because its first cavity is open to the environment. The dual-cavity device also improved the extinction ratio of the reflection spectrum, which is demonstrated in figure 6(b). The first cavity was 35 μm tall and filled with air, leading to a theoretical FSR of 34.32 nm. The polymer cavity was formed by a 56 μm diameter, 20 μm tall disk with a theoretical FSR of 39.94 nm. The device is pictured in figure 6(a). When measured, the air cavity had an average FSR of 36.24 nm and the polymer cavity had an average FSR of 36.07, agreeing within five nanometers of the theoretical values. The high reflected intensity of this device was 68.24 μW , corresponding to a voltage of 468.98 mV, and the low reflected intensity was 1.12

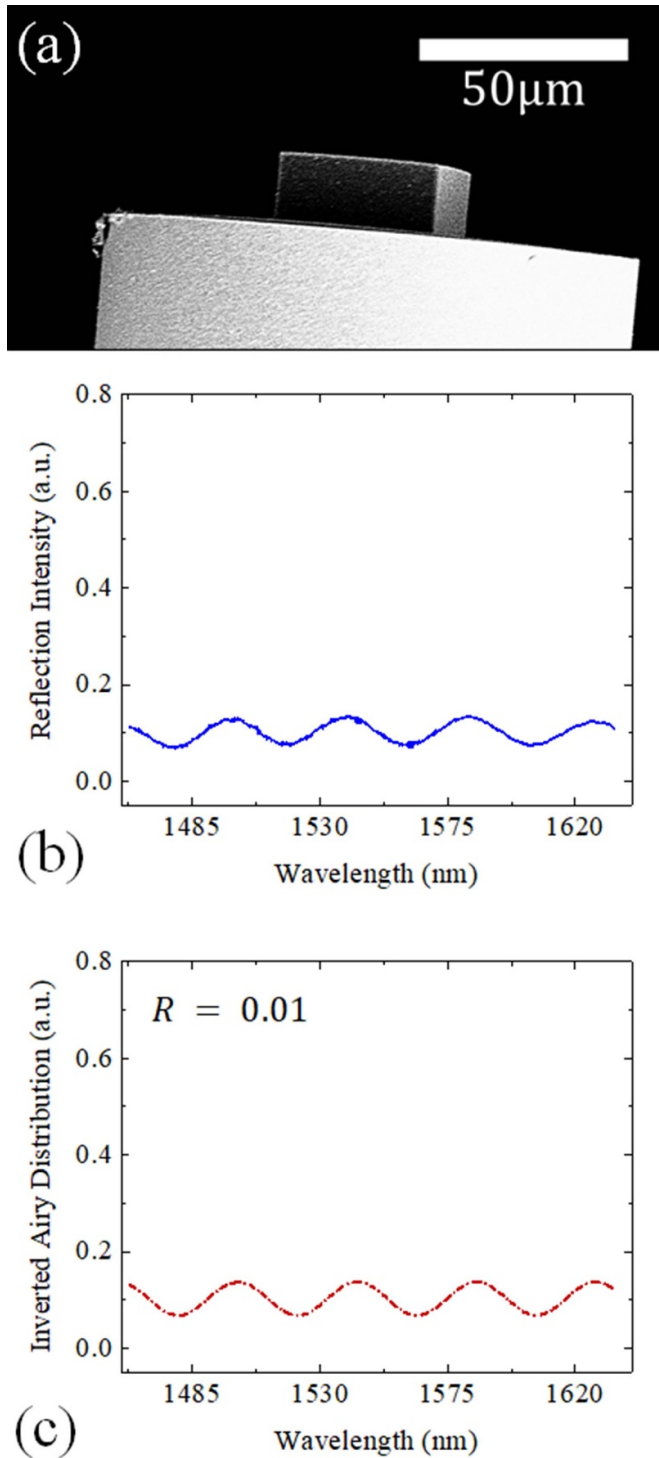


Figure 5. Measurement results from the single-cavity device. (a) SEM image of the device, a 40 μm by 40 μm and 17.58 μm tall rectangle. (b) Measured reflection intensity as a function of wavelength. (c) Airy distribution with $R = 0.01$.

μW reading a voltage of 7.67 mV. This gives the device an extinction ratio of 61. Fitting the Airy distribution, which is included in figure 6(c), yielded a reflectance of 0.3.

Suspending the polymer structure over an air-gap allows various interstitial media to be introduced into the first cavity. Optofluidic dies, quantum dot suspensions, or other gain

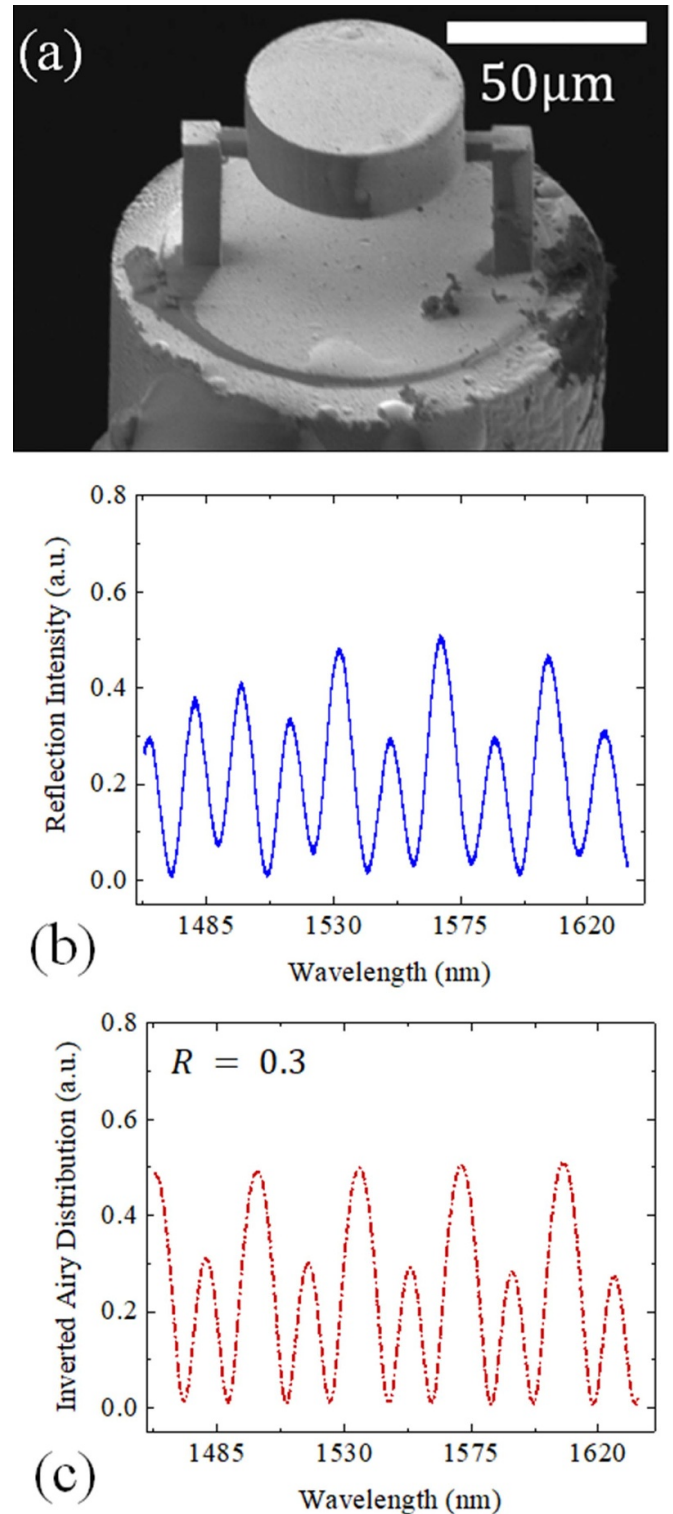


Figure 6. Measurement results from the flat dual-cavity device. (a) SEM image of the dual-cavity device, a 56 μm diameter, 20 μm tall disk suspended above a 35 μm air cavity. These cavity lengths match the hemispherical device. (b) Measured reflection intensity as a function of wavelength. (c) Airy distribution with $R = 0.3$.

media could be inserted to create fiber-tip lasers. The RI of an unknown gas or liquid can also be determined by immersing the dual-cavity device and comparing the shifted FSR to a reference.

Furthermore, by including both a solid polymer cavity and an open cavity, an RI sensor with this device would be self-referencing and temperature immune. If a single open cavity sensor was exposed to both a change in temperature and interstitial medium, the FSR of the device would shift due to the new RI of the cavity, and the new cavity length introduced by thermal expansion of the polymer. It would be very difficult to decouple each effect from the observed FSR shift. The released dual-cavity device would be able to isolate a change in RI from the effect of thermal expansion because the solid cavity would only experience the thermal effects. One could determine the thermal effects from the FSR shift in the polymer cavity, calculate the corresponding effects on the open cavity, and subtracting them from the open cavity FSR shift to isolate the changes in the interstitial medium.

While the dual-cavity device enables many applications, there was a risk that the response from one cavity would interfere with the response from another. If the resonant wavelengths are too close and the width of the resonance is too large, different peaks could not be resolved. Furthermore, light reflected from one cavity could destructively interfere with light resonating in another, removing part of the signal. Fortunately, this kind of interference can be avoided by properly designing the constituent optical cavities. The thickness of all FP cavities and interstitial medium gaps were specifically designed to produce a good number of distinct optical resonances around 1550 nm wavelength. The aforementioned equation of $\Delta\lambda_{\text{FSR}} = \lambda_0^2/2nl$ was used as a theoretical guideline to define the thickness of the polymer cavity and interstitial medium. Peaks from both cavities are clearly resolvable, as seen in figure 6(b), and the extinction ratio improved markedly over the single-cavity device. Since the signal quality improved with the addition of the second cavity, interference between the cavities does not seem to degrade the response.

The hemispherical device enjoys all the utility of the flat dual-cavity device while adding the many benefits of curved mirrors. The hemispherical mirrors reduced diffraction losses and improved lateral confinement to produce a more consistent peak transmission. Within the reflection dips, the flat dual-cavity device showed a variance of 0.53 mV, while the hemispherical counterpart achieved a variance of only 0.026 mV. The hemispherical FP cavity also had the largest extinction ratio observed, with a high reflection intensity of 78.162 μW reading 537.17 mV, and a low reflection intensity of 0.31 μW reading 2.12 mV. This gave the hemispherical device an extinction ratio of 253. An SEM image, and the reflection spectrum of the hemispherical FP cavity are shown in figures 7(a)–(b) respectively. The distance between the center of the inner mirror and the face of the fiber was 35 μm , with a theoretical FSR of 34.32 nm. Within the polymer gap, the concave-convex resonator was 20 μm long between centers for a theoretical FSR of 39.94 nm. The FSR of the air cavity was measured to be 36.31 nm, and the FSR of the polymer cavity was measured to be 36.19 nm. The Airy distribution fit the

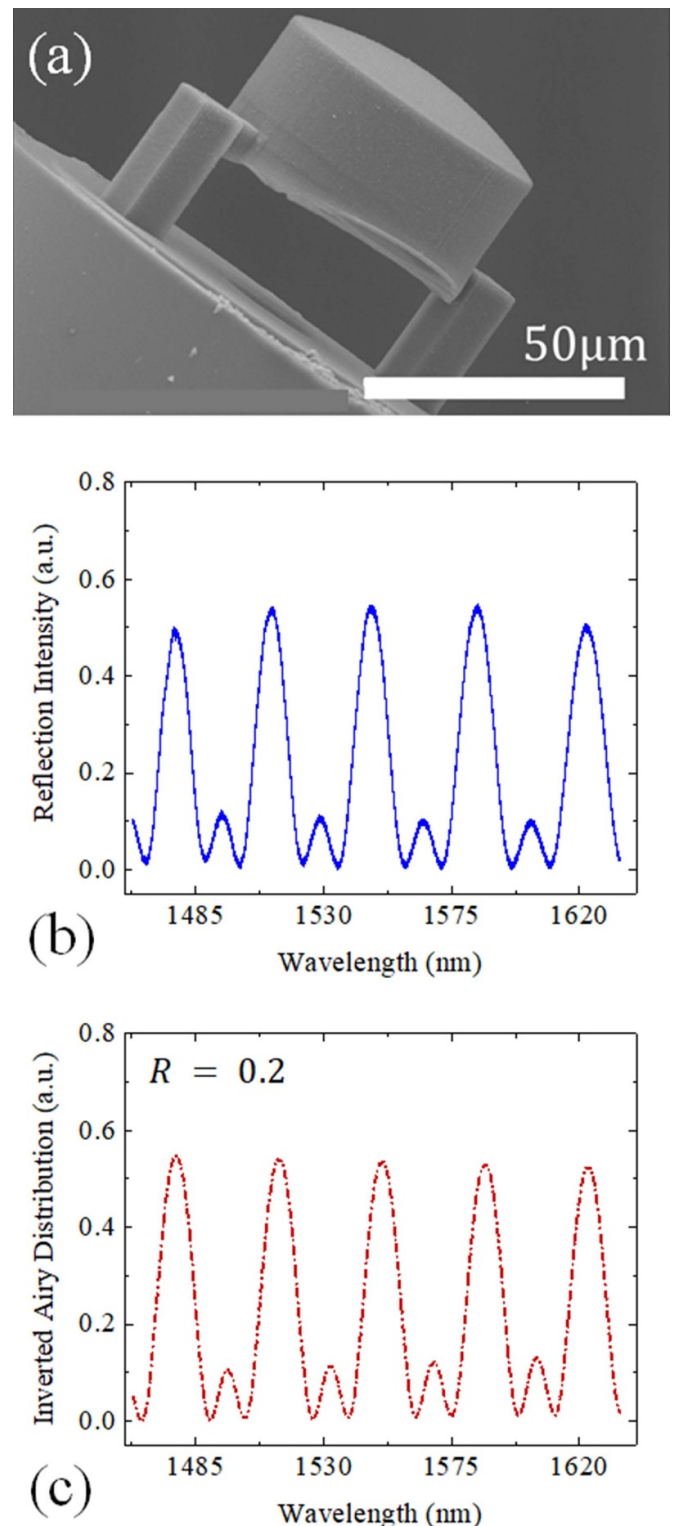


Figure 7. Measurement results from the hemispherical dual-cavity device. (a) SEM image of the device, a 56 μm diameter, 20 μm tall cylinder measured from each center of curvature. The top mirror has a 75 μm radius and the inner mirror has a 35 μm radius. The center of the inner mirror is suspended 22.5 μm above the face of the fiber. (b) Measured reflection intensity as a function of wavelength. (c) Airy distribution with $R = 0.2$.

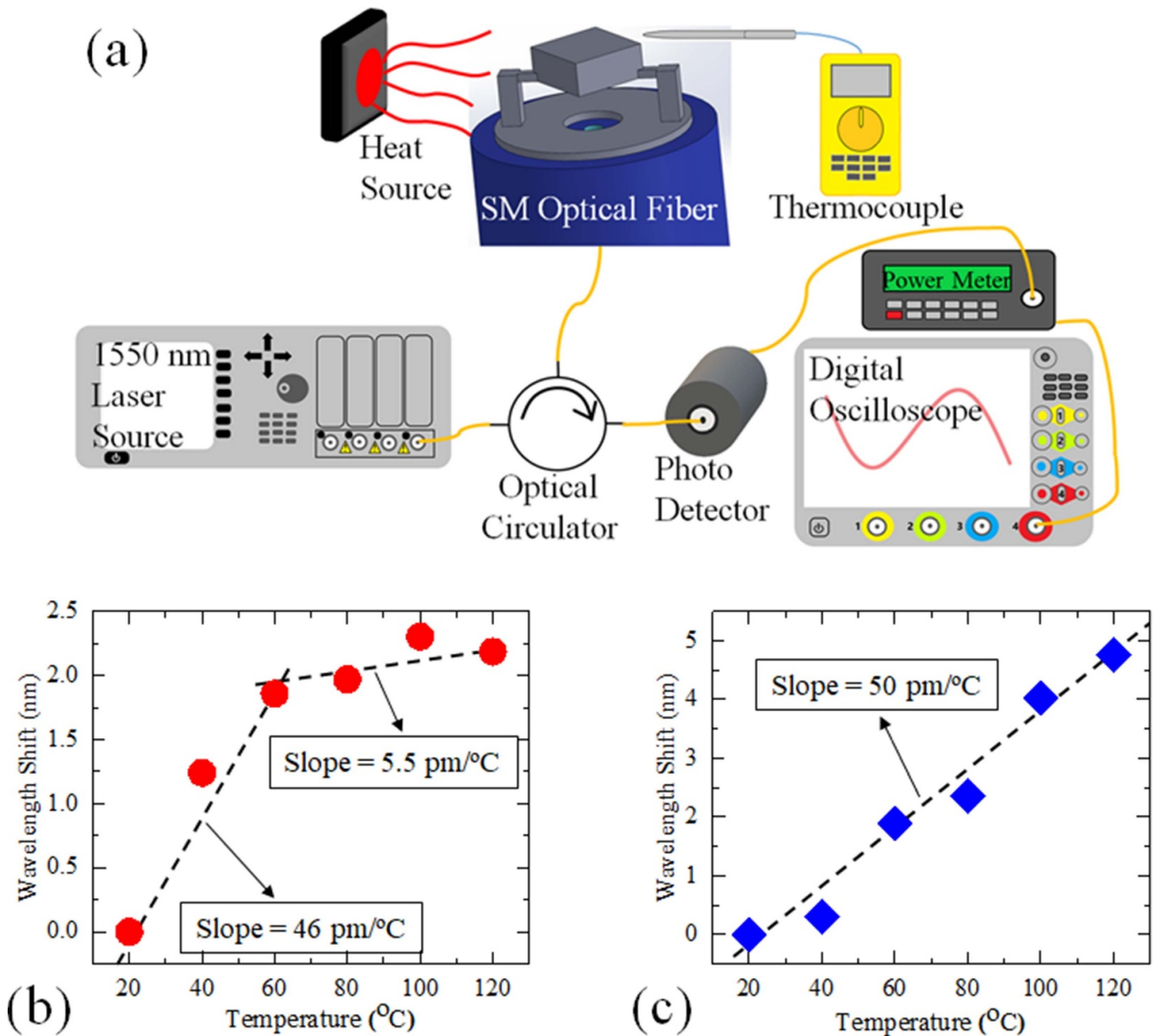


Figure 8. (a) Schematic of the measurement setup to characterize the thermal sensor on an optical fiber tip. (b) Wavelength shifts as responses to temperature variations demonstrated by the single-cavity sensor. (c) Wavelength shifts as responses to temperature variations demonstrated by the flat dual-cavity sensor.

measured response with a reflectance of 0.2. This value is lower than the flat cavity, although the curved mirror reduces losses. The drop is likely caused by the thin polymer feature fabricated over the surface of the fiber. While the feature does not function as intended, as a third curved mirror, the fiber-polymer interface it creates explains the loss in reflectance.

Like all curved-mirror FP cavities, hemispherical resonators are significantly less sensitive to misalignment, making the device more robust in the face of vibrations or impacts to the fiber. In addition, they can be used at higher incident intensities without the loss of resolution that occurs in planar FP cavities. The hemispherical device represents the power of our fabrication technique to utilize 3D freedom to create advantageous geometries that cannot otherwise be realized.

4. Fiber tip 3D remote sensors

The successful outcome of this work will bring a new generation of 3D monolithically integrated multifunctional fiber tip remote sensors that have plethora of applications. As a proof of concept, we characterized the FP resonant wavelength shifts of the single-cavity device (the device shown in figure 5(a)) and the flat dual-cavity device (the device shown in figure 6(a)) due to fluctuations in the surrounding temperature.

As the background temperature changes, the FP resonant wavelength shifts because the cavity undergoes a spectral shift due to the changes in refractive index (thermo-optic effect) and thermal-expansion (thermo-elastic effect) of the sensing material. The changes in resonant wavelength at mode

order m due to thermo-optic and thermo-elastic effects can be expressed as $\Delta\lambda_0/\lambda_0 = \Delta n/n + \Delta l/l$.

The unreleased or single-cavity heat sensor was first characterized according to the measurement setup described in figure 8(a). The unreleased sensor exhibited a linear wavelength shift as a function of temperature with a sensitivity of ~ 46 pm $^{\circ}\text{C}^{-1}$ from 20 to 60 $^{\circ}\text{C}$ and ~ 5.5 pm $^{\circ}\text{C}^{-1}$ from 60 to 120 $^{\circ}\text{C}$ as shown in figure 8(b). The released or dual-cavity heat sensor was then characterized according to the same measurement setup. The released sensor demonstrated a linear wavelength shift as a function of temperature with a sensitivity of ~ 50 pm $^{\circ}\text{C}^{-1}$ from 20 to 120 $^{\circ}\text{C}$ as presented in figure 8(c).

The solidly-mounted sensor showed a linear response up to around 60 $^{\circ}\text{C}$ as shown in figure 8(b). We have performed multiple measurements on the solidly-mounted sensor and obtained very similar results. Our measurements of the solidly-mounted sensors consistently indicated linear responses with slopes range from 45 to 50 pm $^{\circ}\text{C}^{-1}$ and from 5 to 6 pm $^{\circ}\text{C}^{-1}$ for temperature variations from 20 to 60 $^{\circ}\text{C}$ and 60 to 120 $^{\circ}\text{C}$, respectively. We believe this is due to the anchoring scheme of the device. The solidly-mounted sensor was anchored to the fiber tip by the entire bottom of the 3D fabricated structure. This anchoring scheme has limited the linear expansion of the device due to an increase in temperature.

According to the data provided by Nanoscribe GmbH, the thermo-optic coefficient of the IP-DIP is approximately $-2.6 \times 10^{-4}/\text{K}$ at 1550 nm. Using the experimental data and the thermo-optic coefficient of the IP-DIP given by Nanoscribe GmbH, the coefficient of thermal expansion of the IP-DIP was calculated to be $2.9 \times 10^{-4}/\text{K}$.

5. Conclusion

In conclusion, we have demonstrated three FP resonator designs fabricated directly onto the cleaved ends of low-loss optical fibers. Our fabrication technique is simple, fast, and enables true 3D freedom to realize complex features, such as optical elements, which are difficult or impossible to create with traditional microfabrication methods. Two-photon polymerization with ultra-fast laser pulses creates devices on fiber tips in less than 15 min with a single writing step. Each device improved the quality of the FP cavity's reflection response. The single-cavity featured an extinction ratio of 1.90, the released dual planar cavity device obtained an extinction ratio of 61, and the hemispherical cavity device obtained an extinction ratio of 253. The reflectance of the direct fiber-polymer interface was estimated to be 0.01, while the reflectance of IP-DIP was estimated to be between 0.2 and 0.3, both over 1463 nm to 1634 nm. The dual-cavity device promises increased utility as the open cavity is able to interact with its environment and reference changes in RI to the solid cavity. The hemispherical device brings the benefits of a curved-mirror FP resonator such as improved alignment insensitivity and constant resolution at increased intensity, while also providing a consistent resonant intensity across the spectrum of interest.

We have demonstrated the usability of the single-cavity and dual-cavity FP resonators as thermal radiation sensors. Although the single-cavity sensor has a better structural robustness, the dual-cavity sensor has demonstrated a better extinction ratio, thermal sensitivity, and linearity compared to the single-cavity sensor.

These FP cavity devices invite numerous applications, such as on-fiber lasers and various sensors. Our future work specifically hopes to explore reflective coatings to improve the reflectance and quality factor of the reflection spectrum. Micron scale plano and hemispherical cavities with have demonstrated quality factors as high as 10^5 by adding a reflective coating [2], and the next devices we are producing aim to achieve a reflectance of 0.9 or higher. The speed of our fabrication process enables us to take an iterative design approach and explore several reflective coating options. A more reflective FP cavity will have much higher resolution and produce measurable responses for small changes in the RI or length of the cavity to detect different phenomena such as electromagnetic radiations, acoustic waves, temperature and pressure changes, displacements, and hazardous material concentrations in both gas and liquid form. Future work includes determining the suitability of the next generation devices to sense some of these phenomena.

Acknowledgments

The views expressed in this paper are those of the authors and do not reflect the official policy or position of the United States Air Force, Department of Defense, or the US Government. We thank Abigail Juhl and Ecklin Crenshaw for training and assistance with the Nanoscribe, and Richard Johnston and Adam Fritzsche for assistance in the AFIT Nanofabrication and Characterization Facility. This work was funded by the Air Force Office of Scientific Research (AFOSR), Grant F4FGA08338J001.

ORCID iD

Hengky Chandralim  <https://orcid.org/0000-0003-1930-1359>

References

- [1] Wu X, Wang Y, Chen Q, Chen Y-C, Li X, Tong L and Fan X 2019 High-Q, low-mode-volume microsphere-integrated Fabry-Perot cavity for optofluidic lasing applications *Photonics Res.* **7** 50–60
- [2] Wu X, Chen Q, Wang Y, Tan X and Fan X 2019 Stable high-Q bouncing ball modes inside a Fabry-Pérot cavity *ACS Photon.* **6** 2470–8
- [3] Wang W, Zhou C, Zhang T, Chen J, Liu S and Fan X 2015 Optofluidic Laser Array Based on Stable high-Q Fabry-Pérot Microcavities *Lab Chip* **15** 3862–9
- [4] Toninelli C, Delley Y, Stoferle T, Renn A, Gotzinger S and Sandaghdar V 2010 A scanning microcavity for in situ control of single-molecule emission *Appl. Phys. Lett.* **97** 021107

- [5] Hunger D, Deutsch C, Barbour R J, Warburton R J and Reichel J 2012 Laser micro-fabrication of concave, low-roughness features in silica *AIP Adv.* **2** 012119
- [6] Chen Y C, Chen Q, Zhang T, Wang W and Fan X 2017 Versatile tissue lasers based on high-Q Fabry–Pérot microcavities *Lab Chip* **17** 538–48
- [7] Duan X, Huang Y, Agarwal R and Lieber C M 2003 Single-nanowire electrically driven lasers *Nature* **421** 241–4
- [8] Cai H, Liu B, Zhang X M, Liu A Q, Tamil J, Bourouina T and Zhang Q X 2008 A micromachined tunable coupled-cavity laser for wide tuning range and high spectral purity *Opt. Express* **16** 16670–9
- [9] Masson J, St-Gelais R, Poulin A and Peter Y A 2010 Tunable fiber laser using a MEMS-based in plane Fabry–Pérot filter *IEEE J. Quantum Electron.* **46** 1313–9
- [10] Saadany B, Malak M, Kubota M, Marty F, Mita Y, Khalil D and Bourouina T 2006 Free-space tunable and drop optical filters using vertical Bragg mirrors on silicon *IEEE J. Quantum Electron.* **12** 1480–8
- [11] St-Gelais R, Masson J and Peter Y A 2009 All-silicon integrated Fabry–Pérot cavity for volume refractive index measurement in microfluidic systems *Appl. Phys. Lett.* **94** 243905
- [12] Thorpe M J, Balslev-Clausen D, Kirchner M S and Ye J 2008 Cavity-enhanced optical frequency comb spectroscopy: application to human breath analysis *Opt. Express* **16** 2387–97
- [13] Song W Z, Zhang X M, Liu A Q, Lim C S, Yap P H and Hosseini H M M 2006 Refractive index measurement of single living cells using on-chip Fabry–Pérot cavity *Appl. Phys. Lett.* **89** 203901
- [14] Pisani M and Zucco M 2009 Compact imaging spectrometer combining Fourier transform spectroscopy with a Fabry–Perot interferometer *Opt. Express* **17** 8319–31
- [15] Snijders E, Frey J A, Norman J, Post V P, Gossard A C, Bowers J E, van Exter M P, Löffler W and Bouwmeester D 2018 Fiber-coupled cavity-QED source of identical single photons *Phys. Rev. Appl.* **9** 031002
- [16] Colombe Y, Steinmetz T, Dubois G, Linke F, Hunger D and Reichel J 2007 Strong atom–field coupling for Bose–Einstein condensates in an optical cavity on a chip *Nature* **450** 272–6
- [17] Garcia S, Ferri F, Ott K, Reichel J and Long R 2018 Dual-wavelength fiber Fabry–Perot cavities with engineered birefringence *Opt. Express* **26** 22249–63
- [18] Uphoff M, Brekenfeld M, Rempe G and Ritter S 2015 Frequency splitting of polarization eigenmodes in microscopic Fabry–Perot cavities *New J. Phys.* **17** 013053
- [19] Wise S, Mueller G, Reitze D, Tanner D B and Whiting B F 2004 Linewidth-broadened Fabry–Perot cavities within future gravitational wave detectors *Class. Quantum Grav.* **21** S1031–S1036
- [20] Zandi K, Bélanger J A and Peter Y A 2012 Design and demonstration of an in-plane silicon-on-insulator optical MEMS Fabry–Pérot-based accelerometer integrated with channel waveguides *J. Microelectromech. Syst.* **21** 1464–70
- [21] Yao M, Ouyang X, Wu J, Zhang A P, Tam H Y and Wai P K A 2018 Optical fiber-tip sensors based on in-situ μ -printed polymer suspended-microbeams *Sensors* **18** 1825
- [22] Kou J L, Feng J, Ye L, Xu F and Lu Y Q 2010 Miniaturized fiber taper reflective interferometer for high temperature measurement *Opt. Express* **18** 14245–50
- [23] Liu X, Iordachita I I, He X, Taylor R H and Kang J U 2012 Miniature fiber-optic force sensor based on low-coherence Fabry–Pérot interferometry for vitreoretinal microsurgery *Biomed. Opt. Express* **3** 1062–76
- [24] Quan M, Tian J and Yao Y 2015 Ultra-high sensitivity Fabry–Perot interferometer gas refractive index fiber sensor based on photonic crystal fiber and Vernier effect *Opt. Lett.* **40** 4891–4
- [25] Aubry G, Kou Q, Soto-Velasco J, Wang C, Meance S, He J J and Haghiri-Gosnet A M 2011 A multicolor microfluidic droplet dye laser with single mode emission *Appl. Phys. Lett.* **98** 111111
- [26] Gong C-Y, Gong Y, Zhang W-L, Wu Y, Rao Y-J, Peng G-D and Fan X 2008 Fiber optofluidic microlaser with lateral single mode emission *J. Sel. Topics Quantum Electron.* **24** 0900206
- [27] Smith J W, Suelzer J S, Usechak N G, Tondiglia V P and Chandralim H 2019 3-D thermal radiation sensors on optical fiber tips fabricated using ultrashort laser pulses (IEEE) pp 649–52
- [28] Lee K-S, Kim R H, Yang D-Y and Park S H 2008 Advances in 3D nano/microfabrication using two-photon initiated polymerization *Prog. Polym. Sci.* **33** 631
- [29] Ismail N, Kores C C, Geskus D and Pollnau M 2016 Fabry–Pérot resonator: spectral line shapes, generic and related Airy distributions, linewidths, finesses, and performance at low or frequency-dependent reflectivity *Opt. Express* **24** 16366